Nanostructuring and Hardness Evolution in a Medium-Mn Steel Processed by High-Pressure Torsion Technique

Jenő Gubicza,* Moustafa El-Tahawy, Yi Huang, Achintya Kumar Patra, Harald Rösner, Gerhard Wilde, and Subramanya Sarma Vadlamani

Dedicated to Prof. Terence G. Langdon on the occasion of his 85th birthday

Severe plastic deformation (SPD) is performed on a newly developed medium-Mn steel with the composition of Fe–7.66Mn–2Ni–1Si–0.23C–0.05Nb (wt%) to achieve a nanocrystalline microstructure. The SPD process utilizes the high-pressure torsion (HPT) technique, resulting in a nominal shear strain of approximately 36 000% after processing the disk for 10 turns. In X-Ray diffraction line profile analysis, an increase in dislocation density to around $230 \times 10^{14}\,m^{-2}$ is observed. In addition, under high strains, a face-centered cubic (fcc) secondary phase emerges within the body-centered cubic (bcc) matrix. In analytical transmission electron microscopy, using energy-dispersive X-Ray spectroscopy, it is indicated that the secondary-phase particles are enriched in Al, Mn, and Si. As the strain imposed during HPT increases, the simultaneous rise in dislocation density and nanostructuring lead to material hardening. However, the partial phase transformation from bcc to fcc contributes to material softening. As a result of these two opposite effects, the hardness exhibits a non-monotonic variation with the shear strain, displaying, for 10 turns of HPT, a lower hardness compared to fewer turns, despite the continuous increase in dislocation density and decrease in crystallite size.

1. Introduction

Medium-Mn steels which belong to the third generation of advanced high-strength steels are quite promising due to attractive mechanical properties (high strength and good ductility) and lower production cost when compared to the second generation of high-Mn steels.[1,2] Medium-Mn steels typically contain manganese (Mn) within the range of 3–12 wt%, in addition to alloying elements like carbon (C), aluminum (Al), silicon (Si), and micro-alloying elements such as vanadium (V), titanium (Ti), niobium (Nb), and others. These steels have complex multiphase microstructures consisting of retained austenite (RA), α'-martensite, ferrite, and finely distributed carbides.[3] The mechanical behavior of medium-Mn steels mainly depends on the relative amount and stability of RA.[4] The high strength and ductility in these steels can be tailored by carefully designing the alloy chemistry and microstructure to induce transformation-induced plasticity and twinning-induced plasticity effects along with slip activity during deformation.[5] Recently, we developed a medium-Mn steel using a computational thermodynamics computer coupling of phase diagrams and thermochemistry (CALPHAD) approach to develop an RA–ferrite/martensite microstructure with a tensile strength larger than 1 GPa and a

J. Gubicza
Department of Materials Physics
Eötvös Loránd University
P.O.B. 32, H-1518 Budapest, Hungary
E-mail: jeno.gubicza@ttk.elte.hu

M. El-Tahawy
Physics Department
Faculty of Science
Tanta University
Tanta 31527, Egypt

The ORCID identification number(s) for the author(s) of this article can be found under https://doi.org/10.1002/adem.202400920.

Y. Huang
Department of Design and Engineering
Faculty of Science and Technology
Bournemouth University
Poole, Dorset BH12 5BB, UK

Y. Huang
Materials Research Group
Department of Mechanical Engineering
University of Southampton
Southampton SO17 1BJ, UK

A. K. Patra, S. S. Vadlamani
Department of Metallurgical and Materials Engineering
Indian Institute of Technology, Madras
Chennai 600036, India

H. Rösner, G. Wilde
Institut für Materialphysik
Universität Münster
48149 Münster, Germany

total elongation larger than 20%.[6] The reverted austenite is metastable and undergoes a strain-induced martensitic transformation during deformation and provides significant work hardening during tensile/compressive loading.

Severe plastic deformation (SPD) has been widely employed in the last three decades to produce ultrafine grained (UFG) and nanostructured (NS) bulk materials. The SPD-processed materials have significantly higher concentration of vacancies, dislocation densities, and larger fractions of nonequilibrium grain boundaries, which can impart unique properties such as high strength, good ductility, enhanced grain boundary diffusivity, and superplasticity compared to the coarse-grained materials.[7–9] Among the several SPD techniques, high-pressure torsion (HPT) has been shown to be very effective in achieving grain refinement due to the very large shear strain imposed during SPD, which facilitates grain fragmentation resulting in UFG/NS microstructures.[10–15]

The SPD-induced grain refinement in medium-Mn steels has an effect on the phase composition since the grain boundaries may serve as nucleation sites of martensite. Indeed, it was revealed that the martensite phase nucleated at the grain boundaries of the austenite and also at the interfaces between the austenite and ferrite phases during deformation of an UFG medium-Mn steel with the composition of Fe–10.6Mn–0.28Mo–0.08C (in wt%).[16] It has also been demonstrated that the martensite start temperature was lowered by decreasing the grain size; therefore, the stability of the austenite grains depends on the grain size.[17] Severe deformation is an effective tool of grain refinement in medium-Mn steels. For instance, it was reported that the microstructure of the steel containing 8% Mn and 0.08% C was significantly refined via warm rolling, resulting in a grain size of 400 nm for both martensite and austenite phases.[18] A mixture of equiaxed and elongated martensitic ultrafine grains formed in Fe–9.6Ni–7.1Mn (wt%) steel during HPT processing with the average size of about 158 nm while the RA had the grain size of about 28 nm.[19] Post-deformation heat treatment at 600 °C for 7200 s resulted in an increase of the grain size to about 570 nm for martensite and 280 nm for austenite phases.

There are limited studies on the SPD processing of medium-Mn steels.[20–25] Studies on equal-channel angular pressing (ECAP), repetitive corrugation and straightening by rolling, and severe cold rolling on Fe–10Ni–7Mn (wt%) steel have reported a tensile strength of 1 GPa and a ductility of about 15%. It was observed that the SPD processing resulted in a significant fraction of martensite (α′) that underwent a reverse transformation to austenite (γ) after application of a critical strain.[20,21] In contrast, processing by HPT has increased the strength to more than 2 GPa with a ductility of 6–10%, and interestingly only a very small fraction of γ phase has been observed even after 20 turns.[24] During HPT, a part of the mechanical work applied on the sample is converted to heat, resulting in an increase in the specimen temperature which may influence the phase composition. In addition, the applied anvil pressure could contribute to a significant reduction in the equilibrium phase transformation temperature as per the Clausius–Clapeyron equation. The low stacking fault energy of the steel promotes the formation of hexagonal close-packed (hcp) ε-martensite before the reverse austenitic transformation occurs.[21] It was reported that a pressure of 4.3 GPa at room temperature (RT) promotes the transformation of body-centered cubic (bcc) martensite to hcp ε-martensite. Investigations also showed that the hcp ε-martensite is metastable and could transform to face-centered cubic (fcc) austenite upon further straining.[25] From the previous review, it can be noted that HPT processing of medium-Mn steels provides a new pathway to develop steels with the yield strength higher than 2 GPa, and the ductility can be enhanced through microstructural engineering by suitably modifying the composition and process parameters.

In the present study, we performed HPT processing on a newly developed medium-Mn steel of composition Fe–7.66Mn–2Ni–1Si–0.23C–0.05Nb (wt%). The objective is to investigate the evolution of the hardness and the microstructure in the newly developed steel during HPT processing.

2. Experimental Section

2.1. Processing of the Initial Steel Samples and Conditions of HPT

The medium-Mn steel investigated in this present work contained the following elements in addition to the principal component of Fe: 7.66 wt% Mn, 2 wt% Ni, 1 wt% Al, 1 wt% Si, 0.23 wt% C, and 0.05 wt% Nb (see **Table 1**). The chemical analysis of the forged block of steel excluding carbon was made using an inductively coupled plasma-optical emission spectrometer (ICP–OES) (model: 5110, manufacturer: Agilent, USA) while C–S analyzer (model: G4 1CARUS, manufacturer: Bruker, Germany) was used to determine the C and S content. Additionally, the oxygen and nitrogen contents in the studied steel were obtained as 126 and 115 ppm, respectively. For the determination of these concentrations, G8 Galileo mass spectrometer was used (manufacturer: Bruker Co., Billerica, USA). This composition of the medium-Mn steel was designed based on the computational thermodynamics (CALPHAD) approach. The details regarding the principles behind the alloy design and processing can be found in our previous work.[6] Following air induction melting, the cast ingots were homogenized at 1200 °C for 4 h followed by hot forging to 50% reduction to break the as-cast dendritic structure. To erase the prior deformation history, the material was further heat-treated at 1000 °C for 30 min followed by water quenching.

From the forged blocks, disks were cut by electro discharge machining with diameters of 10 mm and thicknesses of ≈0.80 mm. These samples were then processed by HPT technique at RT for 1/4, 1, 3, and 10 turns under quasi-constrained conditions to prevent excessive material flow from around the periphery of the disk in the gap between the upper and lower anvils.[26,27] To perform HPT processing, the disk samples were placed in the sinking of the lower anvil. The upper and lower anvils were brought together to impose an applied pressure of

Table 1. The chemical composition of the studied medium-Mn steel as obtained by ICP–OES.

		Fe	Mn	Al	Si	Ni	C	Nb
Steel composition	Wt%	Balance	7.66	1.04	1.06	1.98	0.23	0.048
	At%	Balance	7.56	2.09	2.05	1.83	1.04	0.030

6.0 GPa, and torsional straining was then achieved by rotating the lower anvil at a rotational speed of 1 rpm.

2.2. Study of the Microstructure of the Initial Material and the Samples Processed by HPT

The microstructure of the initial material was characterized using electron backscatter diffraction (EBSD) in a field-emission scanning electron microscope (SEM) (model: Inspect F, manufacturer: Thermo Fisher FEI, USA) fitted with a high-speed camera (model: Velocity, manufacturer: EDAX) and TexSEM laboratories, orientation imaging microscopy (TSL-OIM) data acquisition and analysis software. For EBSD studies, samples were prepared by mechanical grinding up to 4000 grit SiC paper, followed by polishing with 3 µm diamond paste. The final polishing was performed using a mixture of 70% colloidal silica suspension (particle size: 0.05 µm) and 30% hydrogen peroxide. EBSD scans were performed with a step size of 50 nm.

The microstructure was studied for the initial material and the center and edge parts of the disks processed by HPT using the method of X-Ray line profile analysis (XLPA). The X-Ray diffraction (XRD) patterns were measured by a diffractometer with $CoK\alpha_1$ radiation (wavelength: $\lambda = 0.1789$ nm). A very narrow and parallel X-Ray beam was used which was monochromized with a Ge single-crystal monochromator. The beam had a rectangular shape with a dimension of 0.2×2 mm^2. The scattered X-Ray radiation was detected by 2D imaging plates. The measurement of a full diffraction pattern took 3 d. The intensity at a given scattering angle (2θ) was obtained by integrating the signal along the corresponding Debye–Scherrer ring. The sample surface before XRD experiments was first mechanically polished with 1200, 2500, and 4000 grit SiC abrasive papers and then the polishing was continued with a colloidal silica suspension oxide polishing suspension (OP-S) with a particle size of 40 nm. Finally, the surface was electropolished at 28 V and 0.5 A using an electrolyte with a composition of 70% ethanol, 20% glycerine, and 10% perchloric acid (in vol%).

The parameters of the microstructure were determined from the XRD patterns by the convolutional multiple whole profile (CMWP) fitting method.[28] During CMWP fitting, the diffraction pattern was fitted by the sum of a background spline and the convolution of the instrumental pattern and the theoretical line profiles related to the crystallite size and dislocations. In the HPT-processed samples, the physical broadening of the profiles was much larger than the instrumental broadening and therefore instrumental correction was not applied in the evaluation. The theoretical profile functions related to crystallite size and dislocations are given in ref. [29]. CMWP fitting gave directly the values of the following fitting parameters: the median (m) and the lognormal variance (σ^2) of the crystallite size distribution, the average dislocation density (ρ) and the dislocation arrangement parameter. The latter quantity decreased if the dislocations were arranged into low energy configurations, such as dipoles or low-angle grain boundaries.[29] From the values of m and σ^2, the area-weighted mean crystallite size ($<x>_{area}$) was calculated using the following formula: $<x_{area}> = m \cdot \exp(2.5\ \sigma^2)$.

The microstructures in the initial sample and the disk processed for the highest number of HPT turns were studied by

transmission electron microscopy (TEM). In the latter specimen, both the center and the edge of the disk were investigated. Electron-transparent TEM lamellae were fabricated from representative regions (center and edge) of the HPT disks utilizing focused ion beam milling (model: Crossbeam 340, manufacturer: Carl Zeiss AG, Oberkochen, Germany). Analytical TEM was conducted using an FEI Themis G3 60–300 microscope, which was equipped with various components including a high-brightness field emission gun (X-FEG), a monochromator, an image Cs corrector, an energy-dispersive X-Ray spectroscopy (EDS) system, a high-angle annular dark-field (HAADF) detector (Fischione Model 3000), a fast CMOS camera (Ceta, 4×4 k), and a high-resolution electron energy loss spectrometer (Quantum 965 Gatan Imaging Filter). During the measurements, the microscope operated at an acceleration voltage of 300 kV with an extraction voltage of 3.45 kV for the X-FEG. Dark-field (DF) images were captured using a 10 µm sized objective aperture. Compositional analyses were performed using HAADF scanning TEM (STEM) in combination with EDS with a beam current of 512 pA and a probe size of 0.8 nm, all operated by the Velox software.

2.3. Hardness Testing

The samples were ground and polished for microhardness testing using four grades of abrasive papers: 800, 1200, 2500, and 4000 grit. Subsequently, the samples were further polished using a colloidal silica solution with a particle size of 0.04 µm. The hardness measurements were performed using an FM300 hardness tester equipped with a Vickers indenter with a load of 500 g and a dwell time of 15 s. For the HPT-processed samples, the hardness was measured along the disk diameter, and the spacing between the neighboring indents was 0.5 mm. The experiments were performed at RT. Three indentations were made in the vicinity of each investigated point, and the average hardness values are presented in this study.

3. Results and Discussion

3.1. Microstructure of the Initial Material and the Samples Processed by HPT

The XRD experiment proved that the initial material has a bcc structure with the lattice parameter of 0.2873 ± 0.0001 nm which value did not change significantly during HPT as shown by **Figure 1**a. In this plot, the diffraction patterns taken on the initial sample and the specimens deformed for the lowest and highest strains by HPT (i.e., the center and the edge parts of the disks processed for ¼ and 10 turns, respectively) are shown only. These patterns were measured within the scattering angle range of $2\theta = 40°–130°$. The data between 85° and 95° is absent in the diffractograms because this angular range was hidden by the frames of the imaging plates utilized for detecting the scattered XRD signal. Figure 1a reveals that in addition to the reflections of the main bcc phase, the peaks of an additional fcc phase were also detected in the XRD pattern taken after HPT deformation at high strains, e.g., at the edge of the disk processed for 10 turns. Since the 111 peak of the fcc phase is very close to the 110 reflection of
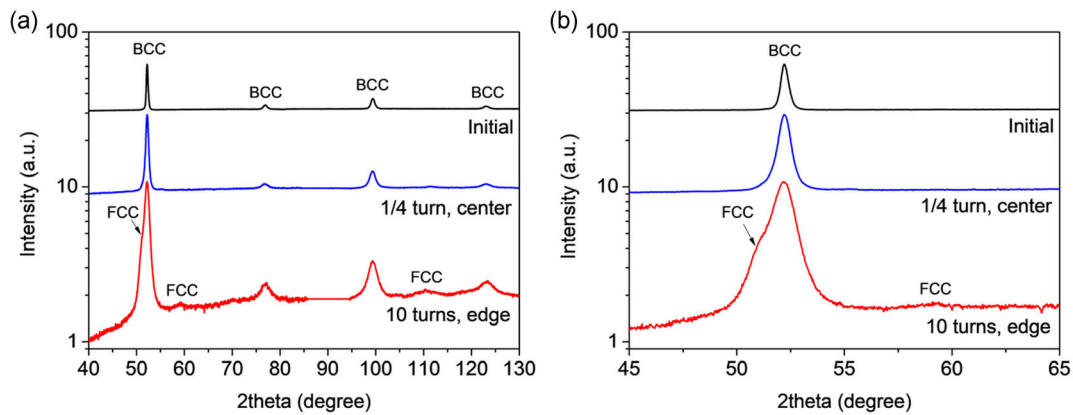
Figure 1. a) Diffraction patterns taken on the initial sample and in the center and the edge parts of the disks processed for ¼ and 10 HPT turns, respectively. b) Enlarged parts of the diffractograms for the diffraction angle ranging between 45° and 65°.
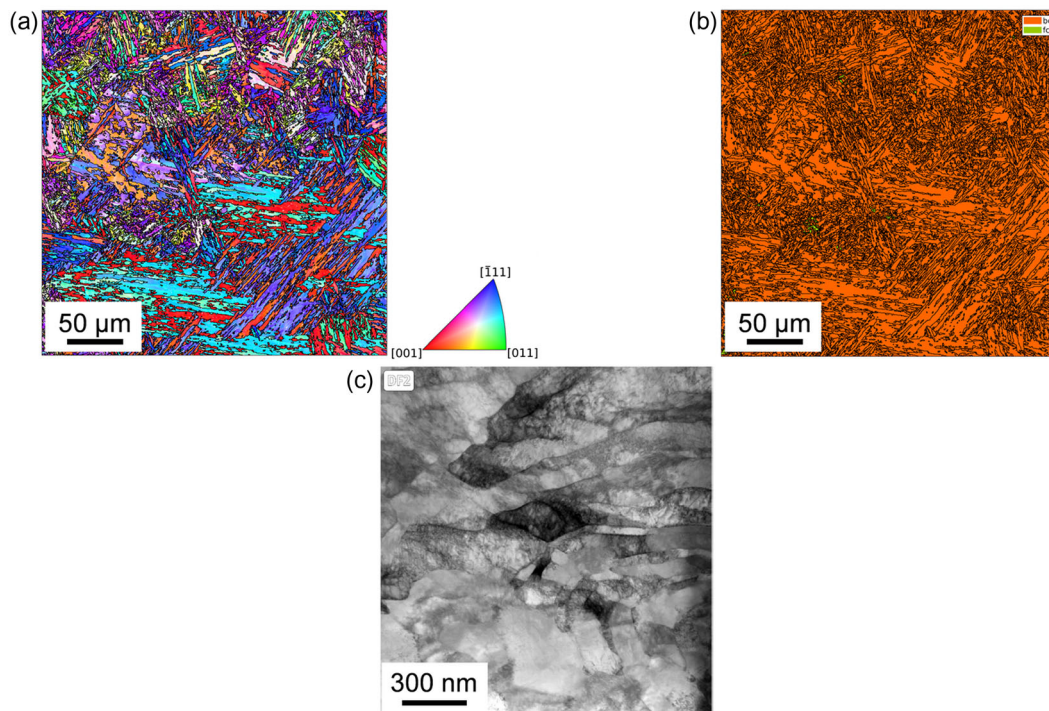

Figure 2. a) EBSD inverse pole figure and b) phase maps obtained by SEM, and c) BF-TEM image taken on the initial steel sample.

the main bcc phase, the former appeared as a shoulder at the left side of the latter one, as shown in Figure 1b.

Figure 2a shows an EBSD image taken on the initial steel, which reveals that the microstructure consists of laths with the thickness varying between 1 and 10 µm and the length of 10–100 µm. The whole initial microstructure in the EBSD micrograph has a bcc crystal structure as indicated by the phase map in Figure 2b, which is in accordance with the XRD result as shown in Figure 1a. The bright-field TEM (BF-TEM) image presented in Figure 2c reveals that the laths are fragmented into grains/subgrains with the size varying between 100 and 300 nm. However, to distinguish in a BF-TEM image between grains and subgrains separated from their neighbors by high- and low-angle

boundaries, respectively, can be challenging with the threshold misorientation angle for high-angle grain boundaries being 15°.

Figure 1 suggests that the width of the XRD peaks of the main bcc phase has increased due to HPT processing. In fact, **Figure 3** shows the full width at half maximum (FWHM) versus the magnitude of the diffraction vector g where these two quantities were calculated as FWHM $= \cos\theta \cdot \Delta(2\theta)/\lambda$ and $g = 2 \cdot \sin\theta/\lambda$ (Williamson–Hall plot). The enhancement of the peak width can be caused by either the reduction of the crystallite size and/or the increase of the dislocation density during the HPT processing. The evolution of the microstructural parameters was determined by XLPA using the CMWP fitting procedure. As an example, **Figure 4** shows the CMWP fitting of the XRD pattern obtained at the edge
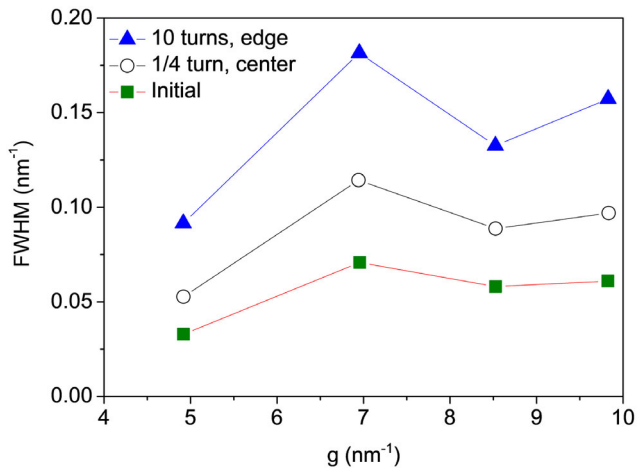
Figure 3. Full width at half maximum (FWHM) versus the magnitude of the diffraction vector g calculated as FWHM $= \cos\theta \cdot \Delta(2\theta)/\lambda$ and $g = 2 \cdot \sin\theta/\lambda$ for the initial sample as well as for the center and the edge parts of the disks processed by ¼ and 10 HPT turns, respectively (Williamson–Hall plot).
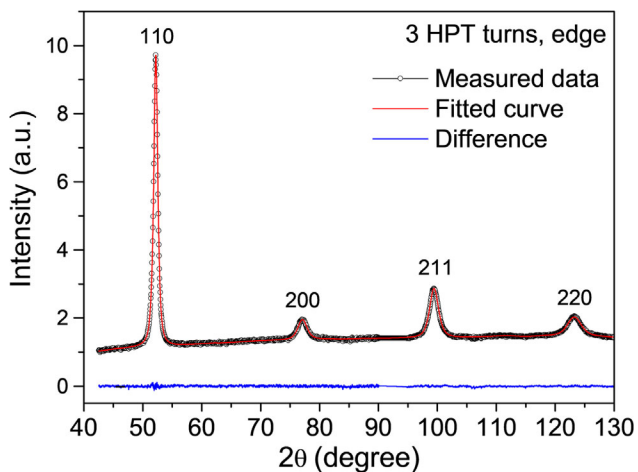
Figure 4. CMWP fitting of the XRD pattern obtained at the edge of the disk processed for 3 turns of HPT. The black open circles and the red solid line represent the measured and the fitted patterns, respectively. The difference between them is indicated by the blue curve at the bottom of the figure.
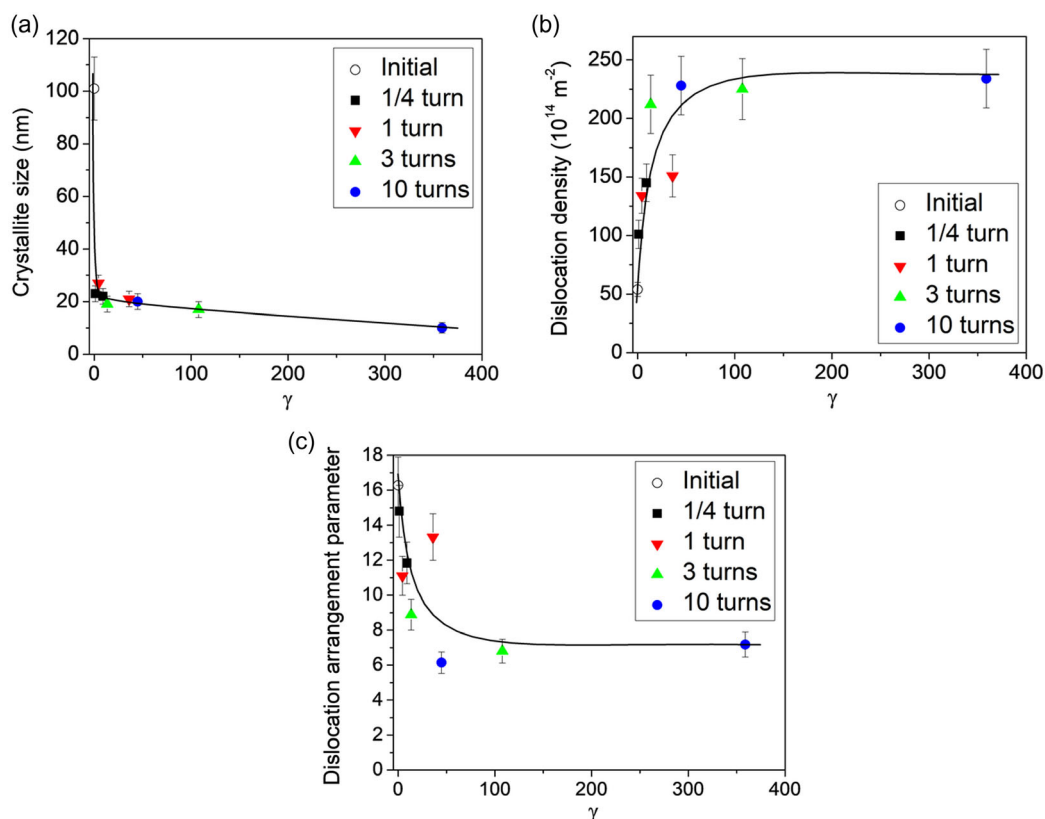
of the disk processed for 3 turns of HPT. The evolution of the crystallite size, the dislocation density, and the dimensionless dislocation arrangement parameter as a function of the nominal shear strain (γ) imposed on the samples during HPT is shown in **Figure 5**. The value of γ was calculated as $\gamma = 2\pi r N/t$, where r and t are the distance from the disk center and the thickness of the sample, respectively, while N is the number of HPT turns.[11] Due to the 2 mm height of the XRD beam, the irradiated area in the disk center spanned the region between $r = 0$ mm and $r = 1$ mm. Therefore, the measurement taken nominally in the center in reality corresponds to an average distance from the center of 0.5 mm. Regarding the XRD pattern measured at the disk

edge, it corresponds to $r = 4$ mm. These values were used to calculate the value of γ in Figure 5.

In Figure 5a, it is revealed that the crystallite size was about 100 nm in the initial material, which corresponds to the size of the grains/subgrains obtained by TEM (as shown in Figure 1c). This value was even reduced to about 20 nm at the nominal shear strain of ≈ 1. Further increasing shear strain yielded a slow gradual decrease in the crystallite size to about 10 nm when the shear strain reached 360. In Figure 5b, it is demonstrated that even for the initial sample prior to HPT, a very high dislocation density with the value of about 54×10^{14} m^{-2} was detected by XLPA, which was probably introduced by the hot forging step in the material processing. The dislocation density further increased with increasing shear strain and got saturated with the value of $\approx 230 \times 10^{14}$ m^{-2} at the shear strain of about 45. It should be noted, however, that the variation of the dislocation density is not monotonous and a value close to the saturation dislocation density ($\approx 200 \times 10^{14}$ m^{-2}) was reached even at a significantly lower strain of about 13. Then, the dislocation density decreased down to $\approx 150 \times 10^{14}$ m^{-2} at the shear strain of about 35, and then increased back to $\approx 230 \times 10^{14}$ m^{-2} when the shear strain increased to ≈ 45. This apparent early saturation of the dislocation density at the shear strains of ≈ 13 was caused by the effect of induced plasticity. Namely, the real shear strain close to the center of the disks is usually higher than the nominal one due to the additional strain induced by the stress field of the high dislocation density formed a little further from the center.[30] Therefore, the shear strains calculated for the edge positions are more reliable. Consequently, it can be stated from Figure 5b that the dislocation density saturated between the shear strains of 50 and 100. The achievement of the minimum value of the dislocation arrangement parameter occurred in the same shear strain range (see Figure 5c). HPT resulted in a decrease of the dislocation arrangement parameter, which was caused most probably by the clustering of dislocations into low energy configurations, such as dipoles and/or low-angle grain boundaries. This trend has also been observed for other SPD-processed metallic materials.[31]

Selected area electron diffraction (SAED) performed in the TEM also confirm the formation of an fcc phase during HPT processing in accordance with the XRD observation. As an example, **Figure 6** shows a BF-TEM micrograph taken at the center of the disk processed by 10 turns of HPT (Figure 6a), the corresponding SAED pattern (Figure 6b), and the azimuthal integration of the diffraction rings (Figure 6c) using software profile analysis of the selected area diffraction patterns (PASAD) tools.[32] The SAED pattern in Figure 6c also shows the coexistence of bcc and fcc phases. Similar results were obtained by SAED performed on the edge of the disk deformed by HPT for 10 turns (not shown here).

Figure 7a,b shows BF- and DF-TEM micrographs obtained at the edge of the disk processed for 10 turns of HPT. The grain size was about 50–100 nm as obtained from the DF image. It should be noted that the grains contained subgrains as revealed by the high contrast differences inside the grains. The subgrain size was estimated from the dimension of the bright spots inside the grains. A grain was magnified in Figure 7b, thereby showing the bright areas whose dimensions varied between 5 and 10 nm. This value is close to the crystallite size determined by XLPA for the edge of the disk processed through 10 turns of HPT (shown

Figure 5. The evolution of a) the crystallite size, b) the dislocation density, and c) the dimensionless dislocation arrangement parameter as a function of the nominal shear strain (γ) imposed on the samples during HPT.
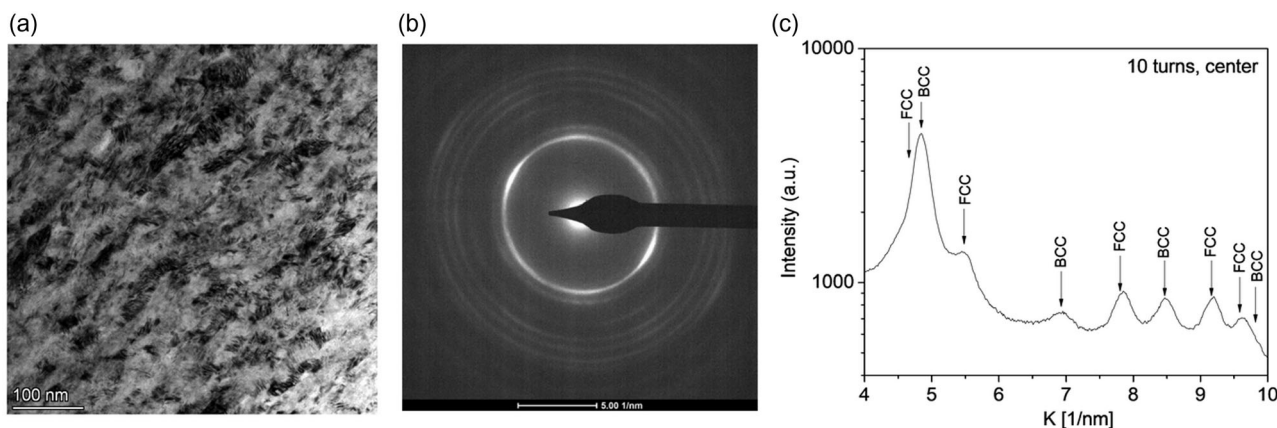
Figure 6. a) BF-TEM micrograph taken at the center of the HPT-processed disk after 10 turns, b) the corresponding SAED pattern and c) the azimuthal integration of the diffraction rings.

in Figure 5a). This result is in accordance with former observations on SPD-processed metallic materials. Namely, previous studies have shown that the crystallite size determined by XLPA is usually considerably smaller than the grain size determined by TEM and rather agrees with the size of subgrains or dislocation cells building up the severely deformed grains.[33] Between the neighboring subgrains, usually there are low misorientations while the grains are separated from their neighbors with high-angle grain boundaries. Since the coherency of the scattered X-rays is broken even by very small misorientations, the crystallite size determined by XLPA corresponds rather to the subgrain size. Thus, the crystallite size is also termed as coherently scattering domain size.[29] A previous DF-TEM study conducted on an HPT-processed Co–Cr–Fe–Ni alloy revealed similar features (bright spots) measuring nanocrystalline grains of about 10 nm in size, akin to our current scenario.[34] Through
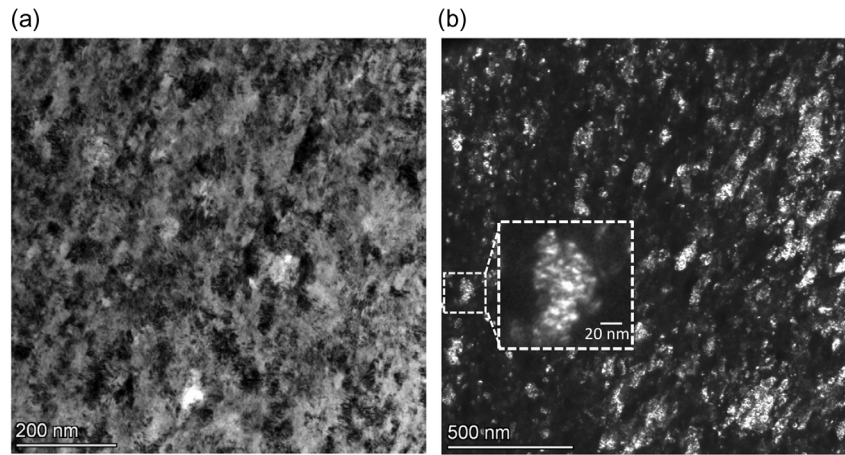
Figure 7. a) BF- and b) DF-TEM micrographs obtained at the edge of the disk processed for 10 turns of HPT. A magnified grain is shown in the dashed white frame in (b) to a better visualization of the subgrains appearing as bright spots inside the grain.

nanobeam diffraction pattern analysis, it was demonstrated that the misorientation angles between adjacent spots did not exceed 2°, indicating that the bright spots within the grains were subgrains. Therefore, even without conducting misorientation analysis on our HPT-processed material, the bright spots with the size of 10 nm in the DF-TEM micrographs are most probably subgrains that are mechanically stabilized under the high strain conditions. Likewise, the alloying elements are crucial in stabilizing this exceptionally fine subgrain structure.

Figure 8 shows an HAADF image and the corresponding Fe, Mn, Al, Si, and Ni elemental maps obtained from STEM–EDS for the edge of the disk processed by 10 turns of HPT. The HAADF micrograph reveals the existence of nano-sized precipitates appearing in dark or bright contrasts, and having a size between 20 and 100 nm. These precipitates are enriched in Al but the concentrations of Mn and Si are also high in some particles. The Fe content of the precipitates is considerably lower than in the matrix, and the Ni concentration is also slightly smaller in the
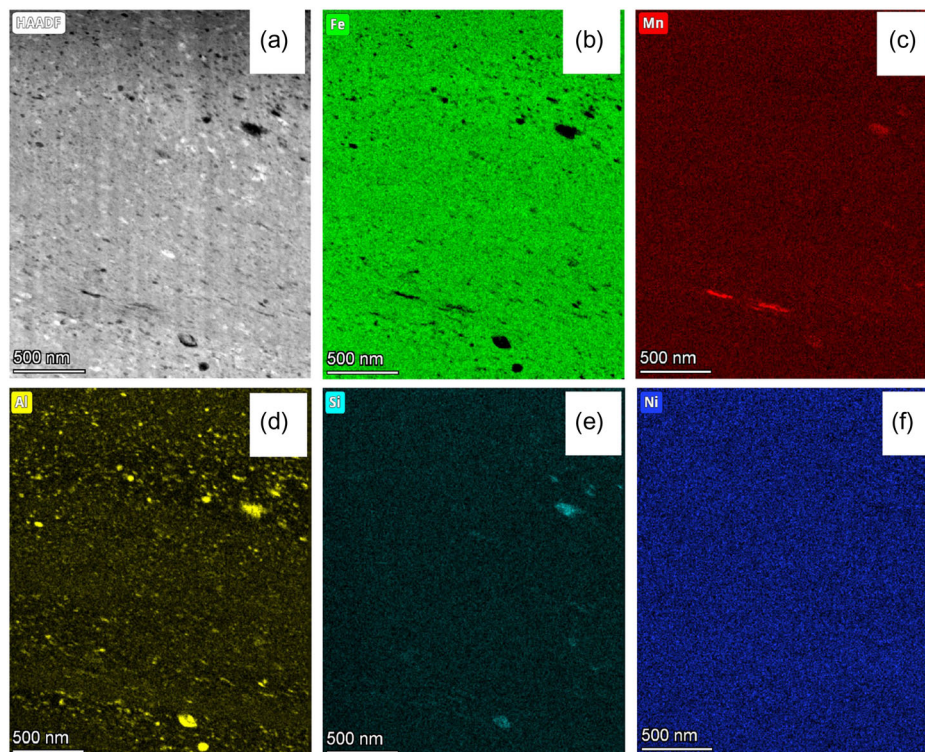
Figure 8. a) HAADF image and the corresponding b) Fe, c) Mn, d) Al, e) Si, and f) Ni elemental maps obtained from TEM–EDS for the edge of the disk processed by 10 turns of HPT.

2400920 (7 of 10)

particles compared to the matrix but the latter one is not clearly visualized in the Ni map (however, this was evident in the quantitative EDS analysis). These precipitates are surely related to the fcc phase observed by both XRD and SAED since other phases were not detected by these diffraction methods (shown in Figure 6). The ratio of the sum of the atomic fractions of Al, Mn, and Si over the same for Fe varied between 0.41 and 2.6 in the precipitates while its nominal average value for the studied steel is 0.16 as can be determined from Table 1. The formation of precipitates within the bcc matrix can result from a multifaceted interplay involving thermal, mechanical, and chemical factors. Materials manufactured using top-down methods like HPT, ECAP, or accumulated roll bonding exhibit various defects, including vacancies, interstitials, dislocations, and grain and twin boundaries introduced during processing. These defects collectively contribute to a complex thermo-mechano-chemical interplay, leading to localized alterations in the atomic structure of internal interfaces. These modifications can impact segregation, the precipitation of grain boundary phases, and their subsequent transformations.[32] In this discussion, we specifically address the influence of temperature bias, given the significant temperature elevation observed during processes like HPT. Indeed, the temperature usually increases in HPT processing since the heat evolved due to plastic deformation cannot be conducted away completely. The temperature rise depends on the applied pressure, rotation speed, and number of turns. For the pressure of 6 GPa and the HPT turn number of 10, the following formula is suggested to use for the calculation of the increase of temperature[35,36]

$$\Delta T = \alpha \cdot HV \cdot \omega \tag{1}$$

where HV is the saturation hardness expressed in MPa, ω is the rotational speed in rpm, and α is a constant varying between 0.0125 and 0.0174 in the different studies.[35,36] Since the saturation hardness is about 8000 MPa for the present steel (shown in **Figure 9**) and the rotation speed is 1 rpm, the temperature rise for 10 HPT turns is about 100–140 °C, i.e., the temperature may increase to 120–160 °C during HPT processing. According to the binary phase diagram of the two components with the highest concentrations (Fe–Mn), a Mn-rich fcc phase can form in the bcc matrix if the Mn content is higher than 4 wt% and the temperature

is higher than 250 °C. In the present case, the temperature increased only up to 120–160 °C during HPT, which is lower than the theoretical threshold temperature of fcc phase formation. In contrast, the studied steel also contains other alloying elements (namely Al, Si, and Ni), which can shift the critical temperature of fcc phase formation to lower values. In addition, the investigated microstructure was not in thermal equilibrium due to the high defect density formed due to HPT processing. Nevertheless, the temperature rise during HPT and the special composition are most probably the main reasons of the observed formation of fcc precipitates. It should also be noticed that former studies have shown that pressure of several gigapascals applied during HPT on steels can contribute to the stabilization of the close-packed phases, such as hcp or fcc.[37,38] Furthermore, it has been reported that additions of Mn and Ni elements significantly reduced the formation pressure of the hcp phase and can prevent it from transforming back during pressure release.[39]

3.2. Hardness Evolution during HPT Processing

Figure 9a shows the hardness versus the distance from the center of the disks processed by HPT for different numbers of turns. The hardness of the initial material was about 4200 MPa which increased to ≈5700 MPa even in the disk center of ¼ turn sample. For the ¼ turn sample, the hardness achieved its highest value of about 8100 MPa at the disk edge. Further increase in the number of turns to one resulted in an increase of the hardness to about 6400 MPa in the disk center while in the other parts the hardness remained unchanged within the experimental error. Significant change in the hardness was not observed between 1 and 3 turns of HPT. In contrast, for 10 turns sample the hardness in the center and the edge decreased to ≈5700 and ≈7000 MPa, respectively. This softening with increasing number of turns can also be seen in Figure 9b where the hardness versus the shear strain is plotted for different numbers of turns. It is evident that the curves obtained for the different numbers of turns do not match. The most striking feature is that the hardness versus shear strain plot obtained for the highest number of turns ($N = 10$) lies below the curves determined for lower numbers of turns. This softening effect was most probably caused by the formation of fcc precipitates in the bcc matrix since: i) the fcc structure is usually
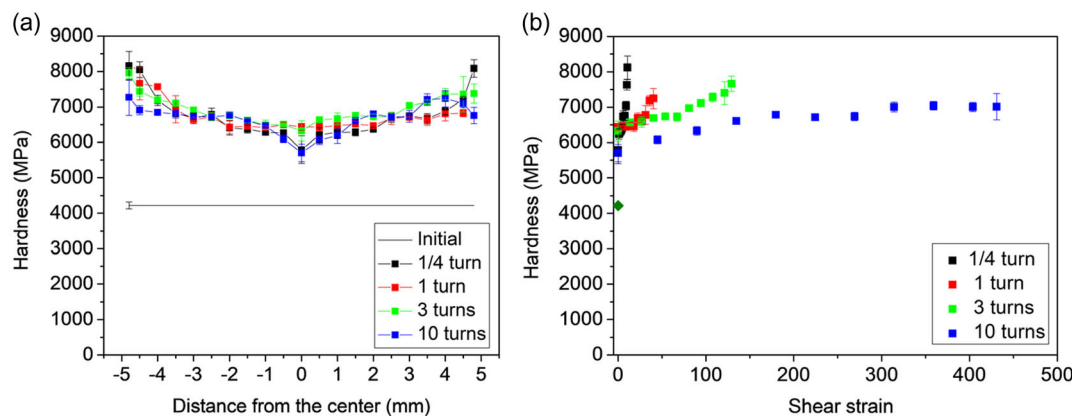
Figure 9. a) The hardness versus the distance from the center of the disks processed by HPT for different numbers of turns. b) The hardness versus the shear strain plotted for different numbers of turns.

**ADVANCED
SCIENCE NEWS**

www.advancedsciencenews.com

**ADVANCED
ENGINEERING
MATERIALS**

www.aem-journal.com

Table 2. The saturation values of the grain size obtained by TEM/EBSD, the crystallite size, and the dislocation density determined by XLPA and the microhardness measured with the load of 500 g for different steels processed by HPT at RT.

| Steel type	Structure	Grain size [nm]	Crystallite size [nm]	Dislocation density [10^{14} m^{-2}]	Hardness [MPa]	References
Ultralow carbon steel	bcc	500	–	–	3600	[42]
Fe–20%Cr–20%Mn–2.6%V–0.3%C–0.8%N	fcc + hcp + V particles	–	–	–	6000	[43]
Interstitial-free steel	bcc	275	80	8	3500	[44]
316 L	fcc	45	21	133	6000	[45]
Fe–12%Cr–1.8%W–1.7%Ni	bcc + particles	140	35	–	6700	[46]
Maraging steel 250	bcc	193	–	–	6900	[47]
Fe–0.1%C	bcc	150	24	55	6500	[48]
Medium-Mn steel	bcc + fcc	50–100	10–20	230	8100	Present study

softer than the bcc one; and ii) the precipitation caused a decrease of the alloying element concentration in the bcc matrix, making dislocation motion easier.

The HPT-induced maximum hardness observed for the presently investigated medium-Mn steel is compared with that determined formerly for other steels listed in **Table 2**. The hardness values vary between 3500 and 8000 MPa. The presently studied steel exhibited an exceptionally high microhardness (about 8100 MPa) among the HPT-processed steels ever investigated. This observation can be attributed to the bcc structure of the matrix which is essentially harder than the fcc structure in austenitic steels, the nanocrystalline microstructure and the very high dislocation density. It is worth noting that the hardness measured for the present HPT-processed medium-Mn steel is exceptional not only compared to conventional materials but also among high-entropy alloy (HEAs) as shown in **Figure 10**. The HEAs usually exhibit an elevated hardness due to the high resistance of the disordered alloy structure against dislocation glide. This is also valid when the HPT-processed HEAs are considered.[40] Figure 10 shows the hardness of HPT-processed materials versus

the initial hardness before HPT deformation for conventional Al, Cu, and Mg alloys; steels; and HEAs. The highest hardness among the HPT-deformed HEAs (about 10 GPa) was obtained for an AlCrFeCoNiNb alloy in which bcc and hexagonal C14 Laves phases coexist with a very small grain size (about 10 nm) and a high dislocation density.[41] It is evident that the presently investigated HPT-processed medium-Mn steel exhibits a hardness (≈8100 MPa) comparable with the hardest HEAs after HPT deformation.

4. Conclusions

From the studies on the effect of HPT processing (up to 10 turns at RT) on the microstructure and hardness of a medium-Mn steel, the following conclusions could be made: 1) The crystallite size and the dislocation density in the bcc matrix saturated with the values of 10–20 nm and ≈230×10^{14} m^{-2}, respectively, at the shear strain of about 45 due to HPT processing. In addition, the dislocations were arranged into low energy configurations with increasing the shear strain imposed during HPT as suggested by the reduction of the dislocation arrangement parameter. Simultaneously, the grain size observed by TEM was refined to 50–100 nm; 2) HPT processing resulted in the formation of precipitates in the bcc matrix which were enriched in Al, Mn, and Si alloying elements. The size of the secondary-phase particles varied between 20 and 100 nm. Most probably, the temperature rise to 120–160 °C during HPT has a significant contribution to the occurrence of precipitation; and 3) The hardness quickly increased up to a very high value of ≈8100 MPa for low shear strain values imposed during HPT, which was due to the nanocrystallization of the microstructure and the increase of the dislocation density. In contrast, at high shear strains, a decrease of the hardness to about 7000 MPa was observed which might be caused by the formation of the softer secondary fcc phase. Nevertheless, the maximum hardness achieved by HPT is exceptionally high among the existing steel compositions.
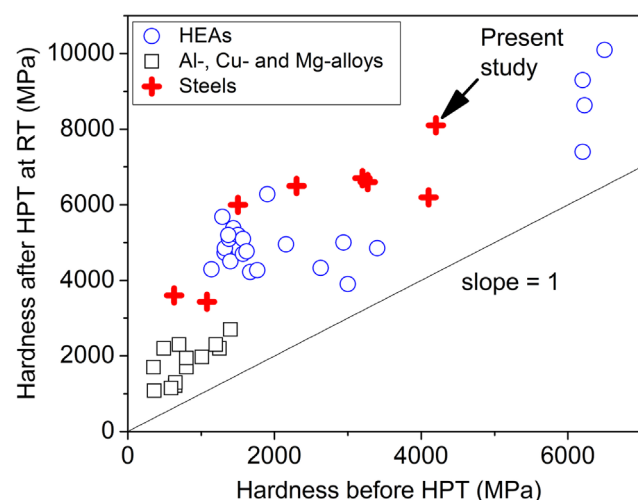
Figure 10. The maximum hardness obtained after HPT-processing at RT versus the hardness before HPT for Al, Cu, and Mg alloys, as well as HEAs and steels.

Acknowledgements

Conflict of Interest

The authors declare no conflict of interest.

Author Contributions

J.G.: conceptualization, validation, formal analysis, resources, writing—original draft preparation, and visualization; M.E.T.: formal analysis, investigation, data curation, and writing—review and editing; Y.H.: methodology, resources, investigation, and writing—review and editing; A.K.P.: formal analysis, investigation, data curation, and writing—original draft preparation; H.R.: methodology, formal analysis, investigation, data curation, writing—review and editing, and visualization; G.W.: validation, resources, and writing—review and editing; S.S.V.: conceptualization, validation, methodology, resources, and writing—original draft preparation.

Data Availability Statement

The data that support the findings of this study are available from the corresponding author upon reasonable request.

[1] D. K. Matlock, J. G. Speer, in *Microstructure and Texture in Steels: and Other Materials* (Eds: A. Haldar, S. Suwas, D. Bhattacharjee), Springer Science & Business Media, London **2009**.

[2] H. Aydin, E. Essadiqi, I. H. Jung, S. Yue, *Mater. Sci. Eng., A* **2013**, *564*, 501.

[3] R. Rana, *Mater. Sci. Technol.* **2019**, *35*, 2039.

[4] R. Rana, P. J. Gibbs, E. De Moor, J. G. Speer, D. K. Matlock, *Steel Res. Int.* **2015**, *86*, 1139.

[5] J. Zhao, Z. Jiang, *Prog. Mater. Sci.* **2018**, *94*, 174.

[6] A. K. Patra, C. N. Athreya, S. Mandal, K. C. H. Kumar, V. S. Sarma, *Mater. Sci. Eng., A* **2021**, *810*, 140756.

[7] R. Z. Valiev, I. Sabirov, A. P. Zhilyaev, T. G. Langdon, *JOM* **2012**, *64*, 1134.

[8] R. Z. Valiev, Y. Estrin, Z. Horita, T. G. Langdon, M. J. Zehetbauer, Y. Zhu, *JOM* **2016**, *68*, 1216.

[9] G. Wilde, S. Divinski, *Mater. Trans.* **2019**, *60*, 1302.

[10] A. P. Zhilyaev, G. V. Nurislamova, B. K. Kim, M. D. Baro, J. A. Szpunar, T. G. Langdon, *Acta Mater.* **2003**, *51*, 753.

[11] A. P. Zhilyaev, T. G. Langdon, *Prog. Mater. Sci.* **2008**, *53*, 893.

[12] A. Hohenwarter, A. Bachmaier, B. Gludovatz, S. Scheriau, R. Pippan, *Int. J. Mater. Res.* **2009**, *100*, 1653.

[13] Y. B. Wang, J. C. Ho, Y. Cao, X. Z. Liao, H. Q. Li, Y. H. Zhao, E. J. Lavernia, S. P. Ringer, Y. T. Zhu, *Appl. Phys. Lett.* **2009**, *94*, 091911.

[14] M. Kawasaki, *J. Mater. Sci.* **2014**, *49*, 18.

[15] J. Gubicza, in *Defect Structure in Nanomaterials*, Woodhead Publishing, Cambridge, UK **2012**.

[16] H. W. Yen, S. W. Ooi, M. Eizadjou, A. Breen, C. Y. Huang, H. K. D. H. Bhadeshia, S. P. Ringer, *Acta Mater.* **2015**, *82*, 100.

[17] E. Jimenez-Melero, N. H. van Dijk, L. Zhao, J. Sietsma, S. E. Offerman, J. P. Wright, S. van der Zwaag, *Acta Mater.* **2009**, *57*, 533.

[18] S. Magalhaes, I. D. Moutinho, I. R. Oliveira, A. O. V. Ferreira, D. S. Alves, D. B. Santos, *ISIJ Int.* **2017**, *57*, 1121.

[19] H. Koohdar, M. Nili-Ahmadabadi, F. J. Kalahroudi, H. R. Jafarian, T. G. Langdon, *JMR&T* **2021**, *15*, 1537.

[20] H. Shirazi, M. Nili-Ahmadabadi, A. Fatehi, S. Hossein Nedjad, *Adv. Mater. Res.* **2009**, *83–86*, 16.

[21] H. Koohdar, M. Nili-Ahmadabadi, M. Habibi-Parsa, H. Ghasemi-Nanesa, *Adv. Mater. Res.* **2013**, *829*, 25.

[22] H. R. Koohdar, M. Nili-Ahmadabadi, M. Habibi-Parsa, H. R. Jafarian, H. Ghasemi-Nanesa, H. Shirazi, *Mater. Sci. Eng., A* **2016**, *658*, 86.

[23] A. Mirsepasi, M. Nili-Ahmadabadi, M. Habibi-Parsa, H. Ghasemi-Nanesa, A. F. Dizaji, *Mater. Sci. Eng., A* **2012**, *551*, 32.

[24] F. J. Kalahroudi, H. Koohdar, H. R. Jafarian, Y. Haung, T. G. Langdon, M. Nili-Ahmadabadi, *Mater. Sci. Eng., A* **2019**, *749*, 27.

[25] H. Ghasemi-Nanesa, M. Nili Ahmadabadi, H. Shirazi, S. H. Nedjad, *Int. J. Mod. Phys.: Conf. Ser.* **2012**, *5*, 9.

[26] R. B. Figueiredo, P. R. Cetlin, T. G. Langdon, *Mater. Sci. Eng., A* **2011**, *528*, 8198.

[27] R. B. Figueiredo, P. H. R. Pereira, M. T. P. Aguilar, P. R. Cetlin, T. G. Langdon, *Acta Mater.* **2012**, *60*, 3190.

[28] G. Ribárik, J. Gubicza, T. Ungár, *Mater. Sci. Eng., A* **2004**, *387–389*, 343.

[29] J. Gubicza, in *X-Ray Line Profile Analysis in Materials Science*, IGI Global, Hershey, PA, USA **2014**.

[30] Y. Estrin, A. Molotnikov, C. H. J. Davies, R. Lapovok, *J. Mech. Phys. Solids* **2008**, *56*, 1186.

[31] J. Stráská, M. Janecek, J. Gubicza, T. Krajnák, E. Y. Yoon, H. S. Kim, *Mater. Sci. Eng., A* **2015**, *625*, 98.

[32] G. Wilde, H. Rösner, S. Divinski, *Mater. Trans.* **2023**, *64*, 1331.

[33] J. Gubicza, *Eur. Phys. J. Spec. Top.* **2022**, *231*, 4153.

[34] H. Jiang, Q. Gong, M. Peterlechner, L. Daum, H. Rösner, G. Wilde, *Mater. Sci. Eng., A* **2024**, *908*, 146758.

[35] K. Edalati, R. Miresmaeili, Z. Horita, H. Kanayama, R. Pippan, *Mater. Sci. Eng., A* **2011**, *528*, 7301.

[36] P. H. R. Pereira, R. B. Figueiredo, Y. Huang, P. R. Cetlin, T. G. Langdon, *Mater. Sci. Eng., A* **2014**, *593*, 185.

[37] S. S. M. Tavares, D. Gunderov, V. Stolyarov, J. M. Neto, *Mater. Sci. Eng., A* **2003**, *358*, 32.

[38] R. B. Figueiredo, F. L. Sicupira, L. R. C. Malheiros, M. Kawasaki, D. B. Santos, T. G. Langdon, *Mater. Sci. Eng., A* **2015**, *625*, 114.

[39] P. M. Giles, A. R. Marder, *Metall. Trans.* **1971**, *2*, 1372.

[40] J. Gubicza, P. T. Hung, *Mater. Trans.* **2023**, *64*, 1284.

[41] P. Edalati, A. Mohammadi, M. Ketabchi, K. Edalati, *J. Alloys Compd.* **2021**, *884*, 161101.

[42] H. Kato, Y. Todaka, M. Umemoto, M. Morisako, M. Hashimoto, M. Haga, *Mater. Trans.* **2012**, *53*, 128.

[43] E. G. Astafurova, M. S. Tukeeva, V. A. Moskvina, N. K. Galchenko, I. A. Bataev, V. A. Bataev, *Lett. Mater.* **2014**, *4*, 269.

[44] J. Cízek, M. Janecek, T. Krajnák, J. Stráská, P. Hruska, J. Gubicza, H. S. Kim, *Acta Mater.* **2016**, *105*, 258.

[45] J. Gubicza, M. El-Tahawy, Y. Huang, H. Choi, H. Choe, J. L. Lábár, T. G. Langdon, *Mater. Sci. Eng., A* **2016**, *657*, 215.

[46] M. V. Karavaeva, M. A. Nikitina, A. V. Ganeev, R. K. Islamgaliev, *IOP Conf. Ser.: Mater. Sci. Eng.* **2017**, *179*, 012037.

[47] K. Jacob, D. Yadav, S. Dixit, A. Hohenwarter, B. N. Jaya, *Mater. Sci. Eng., A* **2021**, *802*, 140665.

[48] D. V. Gunderov, R. N. Asfandiyarov, G. I. Raab, A. A. Churakova, V. V. Astanin, *Lett. Mater.* **2021**, *11*, 416.